Journal of
Biomedical Optics

BiomedicalOptics.SPIEDigitalLibrary.org

Preclinical quantitative *in-vivo* assessment of skin tissue vascularity in radiation-induced fibrosis with optical coherence tomography

Valentin Demidov
Xiao Zhao
Olga Demidova
Hilary Y. M. Pang
Costel Flueraru
Fei-Fei Liu
I. Alex Vitkin

Valentin Demidov, Xiao Zhao, Olga Demidova, Hilary Y. M. Pang, Costel Flueraru, Fei-Fei Liu, I. Alex Vitkin, "Preclinical quantitative *in-vivo* assessment of skin tissue vascularity in radiation-induced fibrosis with optical coherence tomography," *J. Biomed. Opt.* **23**(10), 106003 (2018), doi: 10.1117/1.JBO.23.10.106003.

Journal of Biomedical Optics 23(10), 106003 (October 2018)

Preclinical quantitative *in-vivo* assessment of skin tissue vascularity in radiation-induced fibrosis with optical coherence tomography

Valentin Demidov,[a,*,†] **Xiao Zhao,**[b,†] **Olga Demidova,**[c] **Hilary Y. M. Pang,**[a] **Costel Flueraru,**[d]
Fei-Fei Liu,[a,b,e,f] **and I. Alex Vitkin**[a,e,f]
[a]University of Toronto, Department of Medical Biophysics, Faculty of Medicine, Toronto, Canada
[b]University of Toronto, Department of Otolaryngology - Head and Neck Surgery, Faculty of Medicine, Toronto, Canada
[c]Seneca College, Department of Arts and Science, Toronto, Canada
[d]National Research Council Canada, Information Communication Technology, Ottawa, Canada
[e]University Health Network, Princess Margaret Cancer Centre, Toronto, Canada
[f]University of Toronto, Department of Radiation Oncology, Faculty of Medicine, Toronto, Canada

Abstract. Radiation therapy (RT) is widely and effectively used for cancer treatment but can also cause deleterious side effects, such as a late-toxicity complication called radiation-induced fibrosis (RIF). Accurate diagnosis of RIF requires analysis of histological sections to assess extracellular matrix infiltration. This is invasive, prone to sampling limitations, and thus rarely used; instead, current practice relies on subjective clinical surrogates, including visual observation, palpation, and patient symptomatology questionnaires. This preclinical study demonstrates that functional optical coherence tomography (OCT) is a useful tool for objective noninvasive *in-vivo* assessment and quantification of fibrosis-associated microvascular changes in tissue. Data were collected from murine hind limbs 6 months after 40-Gy single-dose irradiation and compared with nonirradiated contralateral tissues of the same animals. OCT-derived vascular density and average vessel diameter metrics were compared to quantitative vascular analysis of stained histological slides. Results indicate that RIF manifests significant microvascular changes at this time point posttreatment. Abnormal microvascular changes visualized by OCT in this preclinical setting suggest the potential of this label-free high-resolution noninvasive functional imaging methodology for RIF diagnosis and assessment in the context of clinical RT. *© 2018 Society of Photo-Optical Instrumentation Engineers (SPIE)* [DOI: 10.1117/1.JBO.23.10.106003]

Keywords: optical coherence tomography; speckle variance optical coherence tomography; radiotherapy; radiation-induced fibrosis; microcirculation; cancer treatment.

Paper 180293R received May 23, 2018; accepted for publication Sep. 19, 2018; published online Oct. 12, 2018.

1 Introduction

Radiation therapy (RT) is a widely used treatment modality for many cancers. Along with effective treatment outcomes, it is associated with a wide spectrum of negative normal-tissue reactions.[1] One of the most common toxicities is radiation-induced fibrosis (RIF)[2] occurring asymptomatically within months/years following RT.[3] RIF is a condition associated with an increase in collagen deposition in skin and subcutaneous tissues, gastrointestinal tract, lungs, muscles, or other organs,[4–6] leading to parenchymal damage and causing both cosmetic and functional impairment.[7]

Fibrosis development is influenced by multiple factors, including radiation dose, treatment volume, fractionation schedule, genetic susceptibility, and previous treatments.[8–11] As many cancers are treated through the skin, RT interferes with normal proliferation and maturation of basal keratinocytes, hair follicle stem cells, and melanocytes in the skin causing radiation-induced skin changes. Overlapping treatment fields, greater cumulative doses, and larger treated volumes increase total skin irradiation and, therefore, skin toxicity. Large treatment fields are more likely to damage critical mass of epidermal stem cells leading to long-term progressive hardening, edema, modifying microrelief of the skin surface, and causing the changes in dermal thickness.[12] Radiation also damages the vasculature of the dermis, progressively changing superficial blood vessel structure (Fig. 1), and often leading to telangiectasia—a prominent, dilated (enlarged), and tortuous microvasculature near the skin surface.[13]

Basic architecture of the normal human skin is represented by three layers: epidermis, an outermost protective layer 30- to 300-μm thick; dermis, a fibrous layer that supports and strengthens the epidermis; and the subcutis, an insulating fat layer that supplies oxygen and nutrients to the other two layers.[15] The upper $\sim$350 μm of the dermis is the papillary layer containing microvessels supplying the epidermis through so-called capillary tufts.[14] Together with surrounding epidermis and dermis, the microvessel tuft forms the smallest functional unit (FU) of the skin that retains all its charachteristics.[16] Dose response of the FUs defines the RT dose response of the skin,[17] as summarized schematically in Fig. 1. As RT-damaged endothelial cells are not replaced within the tuft after irradiation,[18,19] microvessel ends progressively retract and surviving endothelial cells enlarge to cover the affected area [Figs. 1(b)–1(c)]. This results in partial loss of adjacent basal and dermal cells. At some time point, vessel continuity is broken [Fig. 1(d)] by continued

---

*Address author correspondence to: Valentin Demidov, E-mail: val.demidov@mail.utoronto.ca

†These authors contributed equally to this work.

1083-3668/2018/$25.00 © 2018 SPIE

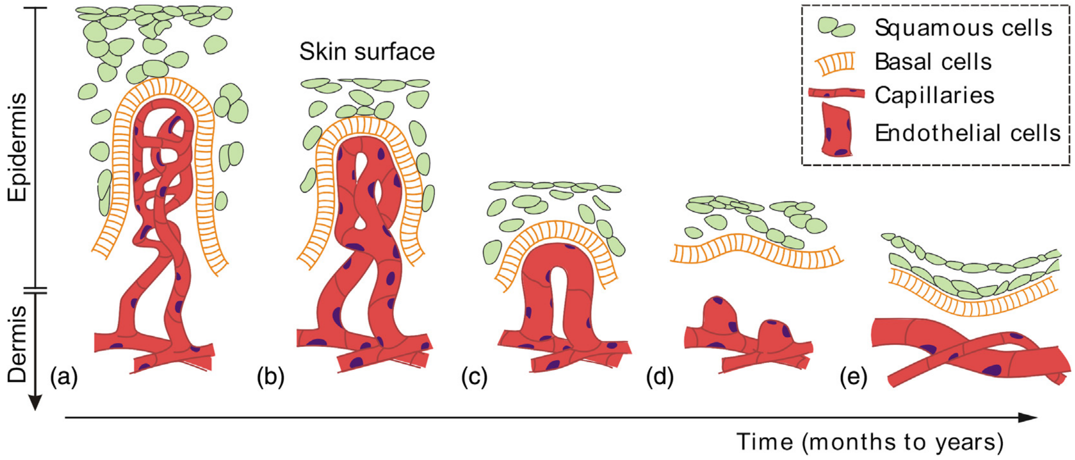

Fig. 1 Schematic diagram of the steps leading to telangiectasia through temporal sequence of skin capillary tuft changes following RT. (a) An FU of healthy skin containing a capillary tuft with associated epidermal and dermal structures; (b)–(d) Progressive retraction and alterations of FU microvessels following irradiation, resulting in partial loss of adjacent basal and dermal cells and leading to (e) telangiectasia formed in the vessels that supplied the tuft (after Ref. 14).

endothelial cell loss, manifesting telangiectasia [Fig. 1(e)] under a thinned epidermis as an area of reddish discoloration with many dilated blood vessels.[20]

Radiation-induced telangiectasia is a common problem in cancer therapy (often associated with RIF), especially in breast and neck, that may be physically disfiguring and psychologically distressing for the patient. Despite the numerous studies of telangectasia, there is a lack of precise data about its incidence,[21] as needed to revert its progression and recover the affected tissues before necrosis.[22,23] This is in part due to the inability of most imaging modalities (e.g., ultrasound, magnetic resonance imaging, and confocal microscopy) to study the dynamic response of microvasculature to RT at the capillary level, either lacking the requisite resolution capability or requiring potentially toxic contrast agents.[24–26] Here, we propose insight into detection of telangectasia in skin RIF using functional optical coherence tomography (OCT). OCT's penetration depth of 1 to 2 mm with micron-scale resolution may represent a useful compromise for dermatological applications. It can image deeper skin structures than confocal microscopy, while maintaining resolution that exceeds that of ultrasound and MRI.[24,25] OCT measures the depth-resolved reflectivity of tissue by detecting backscattered light using the principles of low coherence interferometry.[27] OCT is relatively cheap, fast, noninvasive, and contrast agent free, furnishing essentially "*in-vivo* microscopy" in superficial tissue layers.[28]

In dermatology, OCT contributes to patient management via structural and functional imaging of the epidermal and dermal layers of the skin.[29] OCT images can be used to noninvasively diagnose skin diseases and evaluate their progression longitudinally, as an alternative to skin biopsies or surgical procedures.[30] In assessment of skin late-toxicity fibrosis in response to therapies, OCT has been mostly employed for visualizing orientation, organization, and reflective properties of up-regulated skin collagen—one of the key structural features of fibrotic skin diseases.[31–33] These microstructural collagen-centered studies aside, we propose to take advantage of OCT microangiography for functional assessment of fibrosis. Our overarching hypothesis is that microvascular changes (e.g., telangiectasia) after RT offer biomarkers of radiation-induced skin fibrosis. For its testing, we detect and quantify skin microvascular changes *in-vivo* post-RT with OCT's functional extension called speckle variance OCT (svOCT)[34] and perform histopathologic evaluation to support and validate the OCT observations. For direct comparison of vascular changes in radiation fibrosis to normal tissue vascularity, we consider the 6-month post-RT time point, when fibrosis had clearly developed in the preclinical murine model.

2 Materials and Methods

2.1 *Experiments*

All animal procedures were approved by the Institutional Animal Care and Use Committee of the University Health Network, Toronto, Canada. A 40-Gy dose of ionizing radiation was delivered to the inner left thighs of 7- to 8-week-old C3H wild type female mice ($n = 4$) using a small animal x-ray microirradiator system (XRad225Cx, Precision X-Ray Inc., North Branford, Connecticut) as shown in Fig. 2(a). The system delivered equally weighted parallel-opposed beams (20 Gy dorsally and ventrally) at 225 kVp, 13 mA with added 0.32-mm-thick copper filter, yielding a dose rate output of 2.6 Gy/min though a 2.5-cm-diameter collimator with fluoroscopic guidance. Depth was targeted at 0.5 mm below the skin surface. Given the parallel-opposed beam arrangement and modest murine thigh thickness, there was no appreciable depth dose gradient in the exposed tissue volume. Collimator was used to irradiate only the left thigh, sparing the contralateral right thigh. The irradiator was dosimetrically and geometrically calibrated using controlled tissue phantom methods to ensure accurate dose delivery.[35] Although single dose of 40 Gy is not clinically used (cumulative dose ranges between 50 and 70 Gy, fractionated over 5 to 7 weeks), it was considered appropriate to simulate severe radiation injury and achieve RIF with telangiectasia in mice within first 6 months after treatment, based on previous preclinical experience.[36,37]

A swept-source OCT system based on a quadrature interferometer to suppress the complex conjugate artifact[38,39] was used in this study [Fig. 2(b)]. Its light source (HS2000-HL, Santec, Japan) with 20-kHz rotating-polygon-based tunable filter and wavelength centered at 1320 nm had a sweep range of

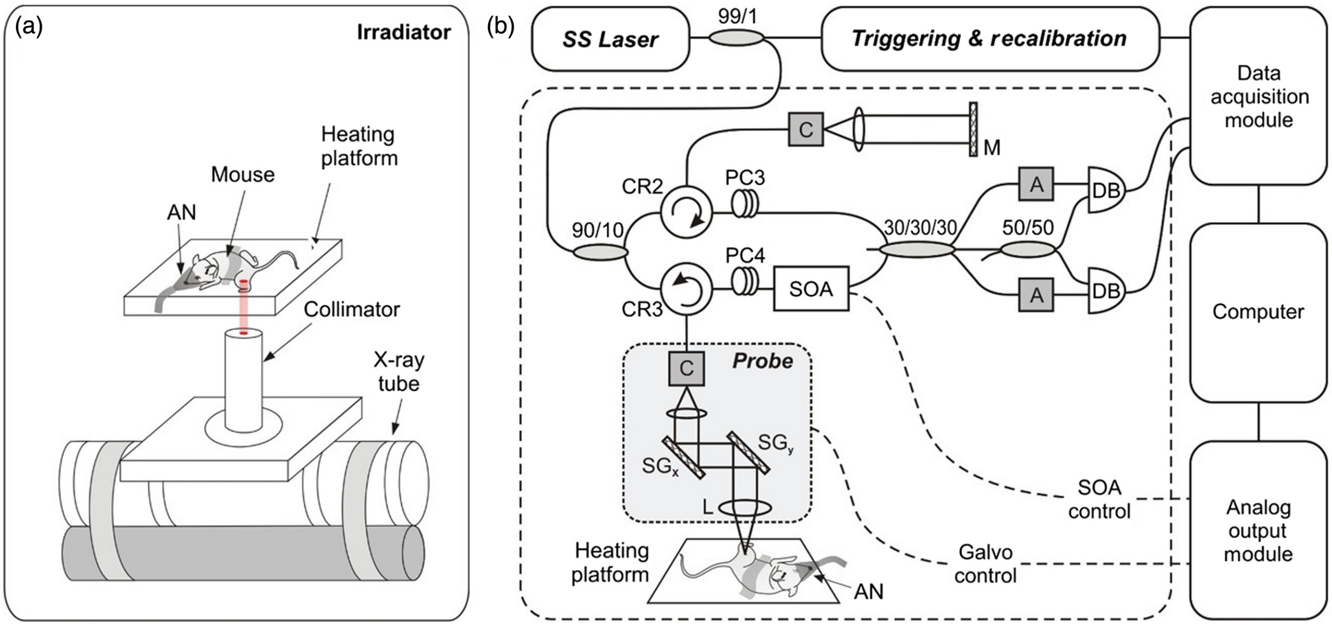

Fig. 2 (a) RT-treatment setup with mouse on a heating platform inside XRad225Cx microirradiator. Mouse was anesthetized and secured to irradiate its left thigh only. A 40-Gy dose was delivered via a pair of parallel-opposed beams. AN, anesthesia nosecone. (b) OCT schematic. PC, polarization controller; CR, circulator; M, mirror; L, lens; C, collimator; SG, scanning galvo; DB, dual balanced photodetector; SS, swept source; A, attenuator; and SOA, semiconductor optical amplifier.

110 nm and an average output power of 10 mW. The axial and lateral resolutions in air were 8 and 15 μm, respectively. OCT optical power at the probe output was measured before each imaging session to be 5 mW, OCT probe imaging angle was set to 86 deg relative to horizontal, and imaging speed was fixed at 40 frames per second.

OCT volumetric images were taken over a $6 \times 3\ \text{mm}^2$ field of view with 800 A-scans per B-scan and a gate length of $N = 8$ (number of sequential same-location B-scans), to enable optimal interframe comparison required for svOCT analysis.[40] The interframe B-scan acquisition rate was chosen to be 25 ms (suitable for stationary tissue speckle to remain correlated between frames, while ensuring complete interframe decorrelation of vascular blood pixels).[41]

Animals were kept in microisolator cages with access to food and water *ad libitum* for 6 months after irradiation prior to OCT imaging. Mice were anesthetized by inhalation of 2% isoflurane and placed under the OCT imaging probe on a heating pad to maintain physiological temperature during imaging procedures. Following imaging, animals were euthanized by anesthesia with ketamine/xylazine followed by cervical dislocation. Thigh tissues from irradiated and contralateral legs were resected, fixed in 10% formalin, embedded in paraffin, and sectioned. Collagen fibers in the skin were labeled with Masson's trichrome staining. Vascular endothelial cells were labeled using CD31 (expressed in endothelial precursor cells) as the primary antibody and 3,3′-diaminobenzidine (DAB; stains nucleic acids) as a chromogen. Slides were counterstained with hematoxylin and scanned by Aperio Scanner (Leica Biosystems, Concord, Ontario).

2.2 Optical Coherence Tomography Signal Processing

Data processing for contrast-agent-free OCT microvasculature visualization is shown in Fig. 3. Skin surface in each B-scan was marked [yellow dashed line in Fig. 3(a)]. Static tissue signal was separated from vascular signal and filtered out using speckle variance equation [Fig. 3(b)]:

$$SV_{zx} = \frac{1}{N} \sum_{i=1}^{N} (I_{izx} - \overline{I_{zx}})^2, \tag{1}$$

where N is the number of B-scans acquired at the same spatial location within a tissue volume, I_{izx} is the intensity of the (z, x)'th pixel of the i'th B-scan, z is the axial coordinate, x is the lateral coordinate, and $\overline{I_{zx}}$ is the mean intensity of i pixels from N consecutive B-scans.

For visual representation, svOCT microvascular images were flattened using skin surface mask [Fig. 3(c)] and depth encoded in RGB color space [Fig. 3(d)]. For depth encoding, microvascular images were first processed using morphological opening/closing algorithm for noise and artifact removal[42] to minimize contributions from nonvessel signals, such as respiratory movement and bulk tissue motion. Datasets were then binarized by applying Otsu's method[43] in depth (z) direction to retain more deep-vessel information in the segmentation, otherwise lost due to OCT signal exponential attenuation with depth. Two hundred and fifty-six color gradations were chosen for depth encoding as shown in Fig. 3(d) color map (green = top layers below the tissue surface and black = deepest tissues).

2.3 Microvasculature Quantification

2.3.1 Histology images

For each animal, 5 to 10 irradiated and nonirradiated immunohistochemically stained tissue sections spaced 300 μm apart were assessed for vascular density and vascular lumen area using CellProfiler (Cambridge, Massachusetts), an open-source cell image analysis software.[44] DAB and hematoxylin components

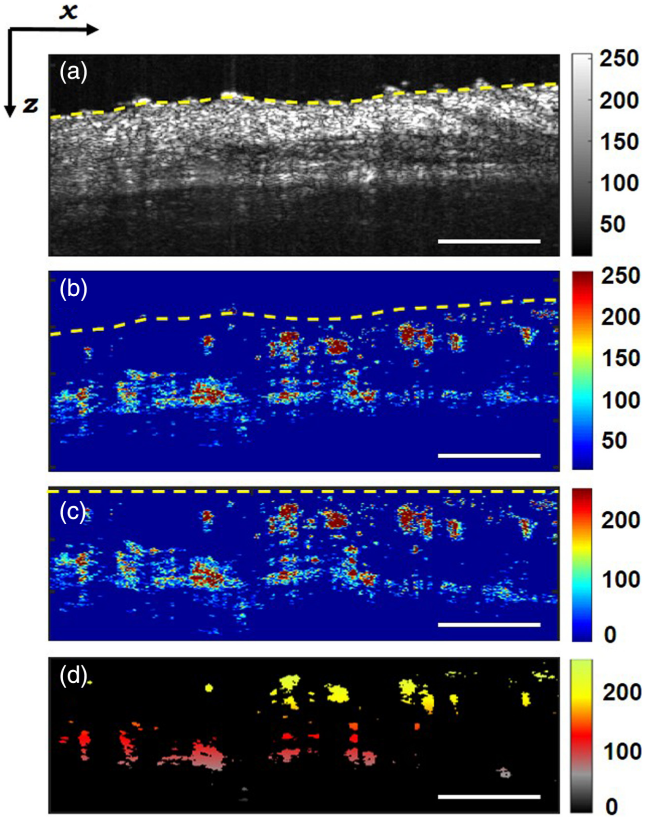

Fig. 3 (a) Structural and (b)–(d) vascular OCT cross sections of irradiated thigh, illustrating signal processing steps. (a) Marking the surface of the skin [labeled in (a)–(c) with yellow dashed line], (b) calculating speckle variance signal, (c) flattening the skin surface for depth encoding, and (d) depth encoding. Scale bars are 0.6 mm. Images are displayed in 8-bit dynamic range with 256 levels (gray and color bars on the right).

in CD31 images were separated following deconvolution procedure. CellProfiler analysis detected image pixels belonging to vessels, which were then counted into vessel area using open-source ImageJ software. Average vessel diameter was then calculated from $A = \frac{\pi d_{\mathrm{avg}}^2}{4}$. The resultant distribution was grouped into 5 μm bins in the 20- to 80-μm-diameter range and plotted as vessel proportion [(quantity of vessels in each diameter bin)/(total number of vessels)] for visualization and comparison with OCT microvascular quantification.

2.3.2 *Optical coherence tomography images*

Each three-dimensional (3-D) OCT scan consisted of 12,000 lateral images to yield 1500 vascular cross sections (12,000/8 images per location) for both irradiated and contralateral legs for each mouse. For comparison with immunohistochemistry, the same average vessel diameter metric was used in OCT data analysis. Vascular pixels were converted to physical dimensions using axial and lateral resolution parameters of the OCT system and average skin refractive index of 1.43.[45] Vessel sizes were tabulated by extracting components from binary vascular images within the chosen diameter range as previously described[46] with 5-μm steps in diameter. All data processing was performed using MATLAB (MathWorks, Massachusetts).

Figure 4 compares the difference in number and location of histological slices and OCT scans analyzed in each animal. Importantly, orders of magnitude more images acquired with OCT than with *ex-vivo* histology provided more data for analysis, yielding more accurate vessel diameter information under realistic *in-vivo* tissue perfusion conditions.

2.4 *Statistics*

Unpaired student *t*-test was used to test for significant differences between irradiated and nonirradiated tissue

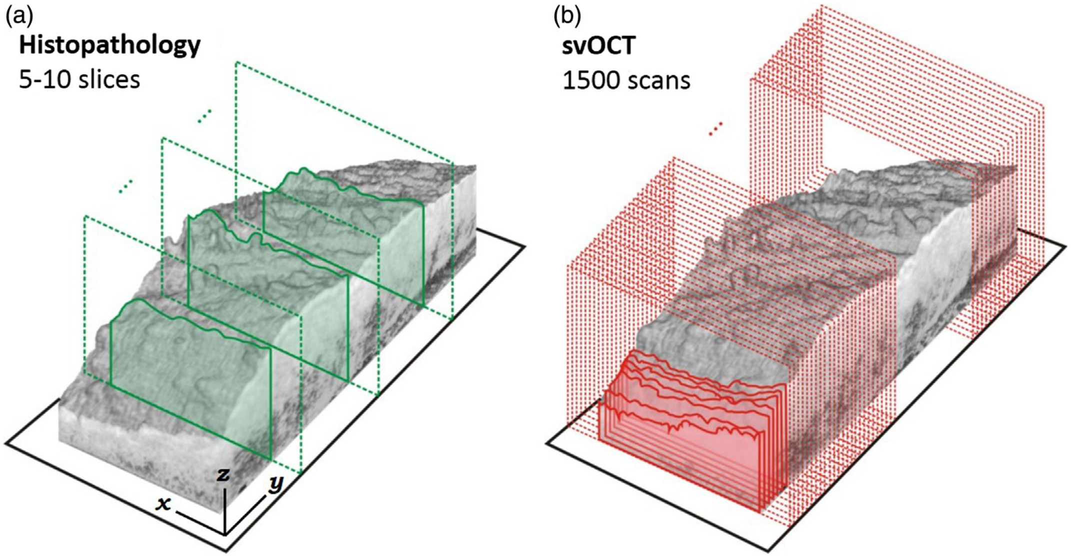

Fig. 4 (a) Schematic orientation of histological sections and (b) OCT scans of tissue. Better microvasculatur quantification accuracy was achieved with OCT, owing to hundreds of lateral cross sections, compared to limited number of *ex-vivo* histological slices from corresponding representative regions. Importantly, OCT images were obtained *in vivo* with functioning vessels, further contributing to accurate vessel diameter estimation.

microvascular parameters. P-value of <0.05 was considered statistically significant.

3 Results and Discussion

Figure 5 shows OCT and Masson's trichrome histological images taken from nonirradiated and irradiated thighs of a C3H mouse, to demonstrate differences in tissue layer organization and distinguish collagen from fatty and muscular tissues. In OCT imaging of normal skin in Fig. 5(a), the dermis D exhibits high scattering as it is composed mainly of connective tissue. This layer can be distinguished from the subcutaneous fat that is more transparent at the OCT wavelength range, thus appearing as a dark layer (labeled with F). The deepest OCT discernible layer is muscle M, appearing brighter due to high scattering of muscle fibers. These layers agree well with the histology shown in Fig. 5(b), where collagen appear in blue, fatty tissue in white, and muscle in red. The subsurface microstructure of fibrotic skin [Figs. 5(c) and 5(d)] demonstrates that the wavy border of the epidermis–dermis junction is replaced by a flat and atrophic epidermis.[47] There is absence of sweat and sebaceous glands, and of hair follicles indicating expected permanent hair loss with radiation doses exceeding 10 Gy.[48,49] Radiation-induced increase in dermal thickness caused by accumulation of collagen and fat as revealed on histology [Fig. 5(d)] prevents OCT light from penetrating further down to the muscle layer (appearing red at the bottom of the trichrome image).

Translation of 3-D svOCT vascular volumes into two-dimensional depth-encoded *en-face* projections of blood vessels enables direct *in-vivo* visual assessment of skin vascular response to radiation. As shown in Figs. 6(a) and 6(b), normal skin capillary tufts [shown schematically in Fig. 1(a)] form the subsurface microvasculature [some are labeled with circles in (a, b)]. In contrast, no capillary tufts are present in irradiated skin [Fig. 6(c) and 6(d)]. Instead, only abnormally aggregated and tortuous vessels—telangiectasias [some are labeled with rectangles in (c, d)] are present in top tissue layers (green-to-yellow colors).

Interestingly, svOCT was unable to detect deeper-located bigger vessels (>100 μm in diameter) in normal skin, possibly due to high scattering of incident OCT light from blood circulating through capillary tufts and from dense hair follicles in the dermal layer.[50] However, in the skin with developed radiation fibrosis, with its thinner epidermis, no tufts, glands, nor hair follicules, bigger vessels located below telangiectasias can be clearly seen [arrows in Figs. 6(c) and 6(d)].

Quantitative assessment of radiation-caused cutaneous microvascular alterations was performed using both OCT and histology. Figure 7 shows svOCT subsurface images of skin microvasculature and hematoxylin—CD31—DAB multistain histological images taken from nonirradiated contralateral and irradiated ipsilateral thighs of a C3H mouse. A typical svOCT cross-sectional image of normal skin [Fig. 7(a)] shows a number of small diameter vessels ($\sim$20 to 50 μm) located in epidermal–

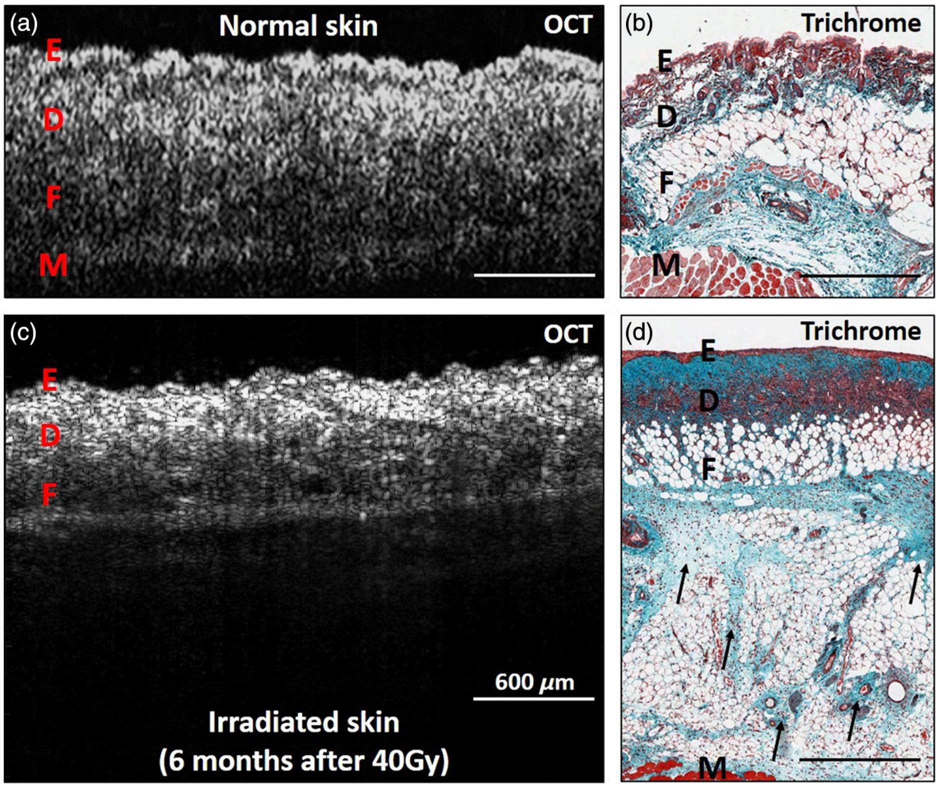

Fig. 5 OCT structural images and Masson's trichrome stains of (a, b) normal and (c, d) irradiated mouse skin. Tissue layers are labeled with E, epidermis; D, dermis; F, fat; and M, muscle. (a, c) Structural OCT imaging shows thinning of epidermal layer, changes in dermal thickness, and modification of microrelief of the skin surface in irradiated skin. In accord with *in-vivo* OCT, (b, d) trichrome histologic staining shows similar trends in skin layer changes and a further increase in collagen deposition [indicated with black arrows on (d)] after irradiation stemming from parenchymal damage to soft tissue. Radiation-induced increase in dermal thickness and reflectivity limits OCT penetration to the deeper muscle layer [appearing red at the bottom of the trichrome image in (d)]. Scale bars are 0.6 mm.

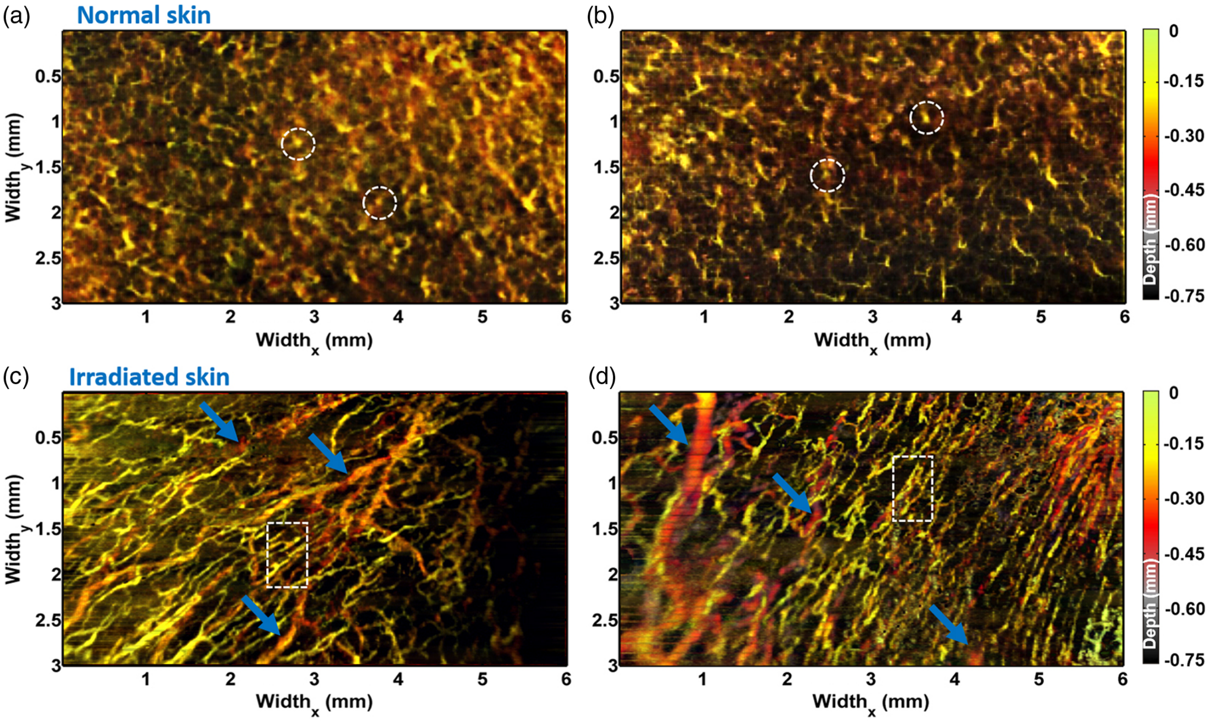

Fig. 6 Typical depth-encoded *en-face* microvascular projections of (a, b) normal and (c, d) irradiated skin (images from both irradiated and nonirradiated thighs of two animals are shown). Capillary tufts [shown schematically in Fig. 1(a)] form the subsurface microvasculature of normal tissue [some labeled with circles in (a, b)]. Note that no capillary tufts are present in irradiated tissue. Instead, only abnormally aggregated and tortuos vessels—telangiectasias [some labeled with rectangles in (c, d)] are present in top tissue layers (green-to-yellow colors). In contrast to normal skin, deeper-located bigger vessels below telangiectasias in irradiated tissues were detected [arrows in (c, d)].

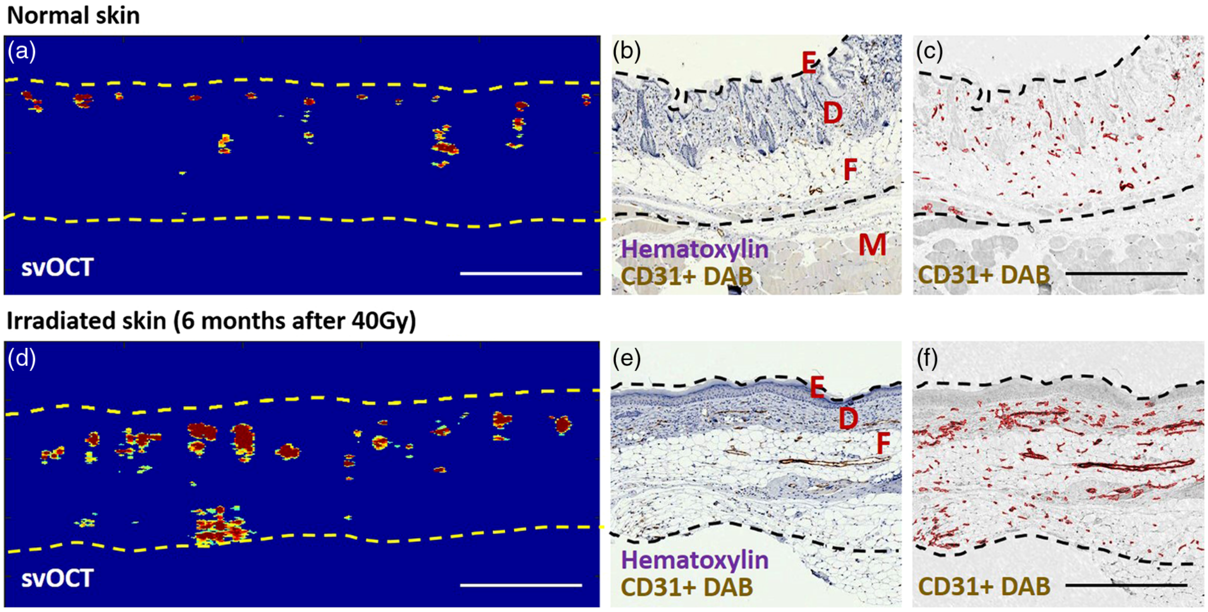

Fig. 7 Vascular cross sections of normal (top row) and irradiated (bottom row) mouse thigh skin. Regions between the skin surface and 650-μm depth were chosen for microvascular area quantification (dashed lines on both svOCT and histology slides): (a, d) vascular cross section obtained with svOCT, (b, e) hematoxylin, CD31, and DAB staining. Tissue layers are labeled with E, epidermis; D, dermis; F, fat; and M, muscle, and (c, f) DAB and hematoxylin components in CD31 images were filtered out using a deconvolution procedure to enhance histological microvessel visualization. Scale bars are 0.6 mm.

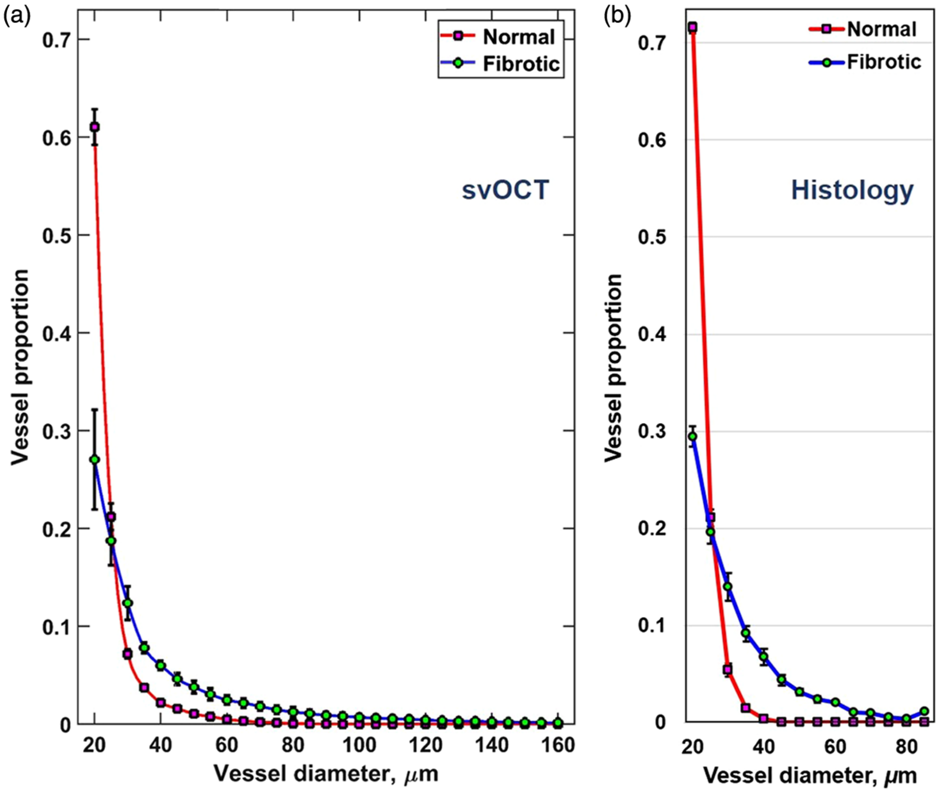

Fig. 8 Microvasculature quantified by vessel diameter, with 5-μm bin steps for (a) OCT and (b) histology. Vessel proportion is plotted as (quantity of vessels in each diameter bin)/(total number of vessels), with the area under each corresponding curve equal to unity. Both plots show similar trends, specifically (1) the number of small capillaries is ∼2× smaller in irradiated fibrostic skin compared to unirradiated controls and (2) blood vessels of larger ∼30- to 80-μm diameters prevail in fibrotic tissue [∼50% (OCT) and 45% (histology), compared to ∼20% (OCT) and 10% (histology) in normal skin]. Symbols are experimental points, and lines are a guide for the eye. Error bars represent mean ± standard deviation.

dermal junction region. These represent healthy skin FUs with average vessel diameter of ∼30 μm.[15] As the normal skin thickness in C3H mice is 600 to 700 μm, the range of surface to depth of 650 μm was chosen for the evaluation purposes (yellow dashed lines). Tissue layers are labeled with E (epidermis), D (dermis), F (fat), and M (muscle) in the corresponding multistain histology cross section [Fig. 7(b)]. Filtering out hematoxylin component with CellProfiler and labeling vascular lumens within the selected 650-μm depth range [black dashed lines in Fig. 7(c)] allowed for histological quantification of microvasculature with high resolution, to compare with/validate the svOCT results. Note that in contrast to normal mouse thigh skin, irradiated skin tissue shows more irregular blood vessel capillary distribution, with substantial preponderance of larger vessels [Figs. 7(d)–7(f)].

To compare the distributions of normal and fibrotic skin vessel diameters, we display vessel proportions categorized by vessel diameter within 5-μm-wide diameter bins for both OCT and histology (Fig. 8). Vessel proportion is plotted as (quantity of vessels in each diameter bin)/(total number of vessels), with the area under each corresponding curve equal to unity. As seen, both plots in the figure exhibit similar trends, demonstrating that the number of smaller microvessels is ∼2× lower in irradiated skin. These trends are in accord with previous histological observations in rats following 30- to 50-Gy single-dose irradiations[51] and are consistent with microvascular dilation characteristic of telangiectasia. Further, both imaging methods consistently quantified the prevalence of blood vessels of larger diameters (>30 μm) in fibrotic skin. svOCT *in-vivo* analysis of larger vessels revealed that ∼20% belongs to ∼30- to 80-μm-diameter range in normal skin, increasing to ∼50% in fibrotic skin. Histological quantification showed comparable numbers of ∼10% and 45%, respectively. Presence of telangiectasia in top fibrotic skin layers and deeper-located bigger vessels substantially changed the corresponding vessel proportions, compared to values obtained for normal skin. Statistical analysis of results, performed separately for OCT and histology, showed 0.00001 to 0.01 P-values for all vessel diameters, except those in 25-μm-diameter range ("normal" and "fibrotic" curve cross points in both plots).

Changes in vessel size distribution may serve as a useful functional imaging biomarker in assessment of late radiation toxicity in RIF. Moving forward, longitudinal monitoring of tissue vascularity is needed to study changes in these proportions during fibrosis development following irradiation. This will elucidate the temporal trajectory of microvascular alterations post-RT, for potential correlation and mechanistic insights relative to the progression of microstructural remodeling characteristics of fibrosis. If microvascular changes prove earlier and more sensitive/robust as radiation response metrics, such early fibrosis detection may help in personalized management of this serious late RT toxicity.[22,23]

Similar functional OCT approaches are being investigated for detection, quantification, and management of early RT toxicities as well, for example in intrafraction monitoring of mucositis development in superficial mucosal layers of the oral cavity of head and neck radiotherapy patients.[52–54] Further, skin is indeed a very important target of such RT imaging studies, given its clinical importance as a dose-limiting organ and thus common occurrence of RIF. However, its thicker structures in humans compared to mice may somewhat limit clinical utility, as OCT can only detect important RIF changes within ∼1 mm of the skin surface (unless optical clearing is used, a promising practical solution to this obstacle),[55] thus its application should be driven by relevant tissue changes within this depth range. Nevertheless, given the current lack of quantifiable objective measurements of skin fibrosis, OCT's ability to detect microstructural and microvascular alterations within ∼1-mm-depth range (thus encompassing important alterations throughout the epidermis and some of the underlying dermis) has great potential to become a valuable tool for RIF diagnosis, prognosis, and management in the clinic.

4 Conclusion

Radiotherapy is a major and effective treatment modality for many cancers but can also cause unwanted long-term toxicities, such as fibrosis that occurs within months/years following the treatment. Radiation damage in skin is associated with telangiectasia and is a common problem in RT, especially in breast and neck, that is difficult to reliably detect and effectively manage. We demonstrate the use of functional *in-vivo* OCT for visualizing and quantifying RIF-associated microvascular changes, and suggest the evaluation of its potential utility for early detection and effective management of RT-induced fibrosis. Our pilot preclinical study demonstrates that OCT is capable of capturing the subtle underlying vascular differences between normal and fibrotic tissues *in vivo*, suggesting that changes in vessel size proportions may serve as an important functional imaging biomarker in assessment of late RT skin toxicity. Future work will examine the generalizability of these results in other preclinical *in-vivo* models of RT fibrosis, longitudinally explore temporal changes in tissue vascularity during the course of RIF development, and expand into pilot clinical studies of microvascular radiotherapeutic monitoring.

Disclosures

The authors declare no conflicts of interest.

Acknowledgments

The OCT system was developed at the National Research Council of Canada with contributions from Dr. Linda Mao, Dr. Shoude Chang, Dr. Sherif Sherif, and Dr. Erroll Murdock. This study was supported by the Canadian Institutes of Health Research (I.A.V), the Natural Sciences and Engineering Research Council of Canada (V.D.), and the Ontario Student Assistance Program (O.D.).

References

1. S. M. Bentzen et al., "Normal tissue effects: reporting and analysis," *Semin. Radiat. Oncol.* **13**(3), 189–202 (2003).
2. A. J. Van der Kogel, "Radiobiology of normal tissues," in *Basic Clinical Radiobiology*, G. G. Steel, Ed., pp. 99–107, Arnold, London (1993).
3. B. O'Sullivan and W. Levin, "Late radiation-related fibrosis: pathogenesis, manifestations, and current management," *Semin. Radiat. Oncol.* **13**(3), 274–289 (2003).
4. C. N. Andreassen et al., "ATM sequence variants and risk of radiation-induced subcutaneous fibrosis after postmastectomy radiotherapy," *Int. J. Radiat. Oncol. Biol. Phys.* **64**(3), 776–783 (2006).
5. L. R. Coia, R. J. Myerson, and J. E. Tepper, "Late effects of radiation therapy on the gastrointestinal tract," *Int. J. Radiat. Oncol. Biol. Phys.* **31**(5), 1213–1236 (1995).
6. T. Holscher, S. M. Bentzen, and M. Baumann, "Influence of connective tissue diseases on the expression of radiation side effects: a systematic review," *Radiother. Oncol.* **78**(2), 123–130 (2006).
7. J. M. Straub et al., "Radiation-induced fibrosis: mechanisms and implications for therapy," *J. Cancer Res. Clin. Oncol.* **141**(11), 1985–1994 (2015).
8. A. M. Davis et al., "Late radiation morbidity following randomization to preoperative versus postoperative radiotherapy in extremity soft tissue sarcoma," *Radiother. Oncol.* **75**(1), 48–53 (2005).
9. F. B. Geara et al., "Factors influencing the development of lung fibrosis after chemoradiation for small cell carcinoma of the lung: evidence for inherent interindividual variation," *Int. J. Radiat. Oncol. Biol. Phys.* **41**(2), 279–286 (1998).
10. M. V. Graham et al., "Clinical dose-volume histogram analysis for pneumonitis after 3D treatment for non-small cell lung cancer (NSCLC)," *Int. J. Radiat. Oncol. Biol. Phys.* **45**(2), 323–329 (1999).
11. S. Collette et al., "Predictors of the risk of fibrosis at 10 years after breast conserving therapy for early breast cancer: a study based on the EORTC Trial 22881-10882 'boost versus no boost'," *Eur. J. Cancer* **44**(17), 2587–2599 (2008).
12. J. F. Bourgeois et al., "Radiation-induced skin fibrosis after treatment of breast cancer: profilometric analysis," *Skin Res. Technol.* **9**(1), 39–42 (2003).
13. A. B. Cognetta, *Radiation Therapy for Skin Cancer*, W. M. Mendenhall, Ed., Springer, New York (2013).
14. J. O. Archambeau, R. F. Zner, and T. Wasserman, "Pathophysiology of irradiated skin and breast," *Int. J. Radiat. Oncol. Biol. Phys.* **31**(5), 1171–1185 (1995).
15. J. O. Archambeau, "Integumentary system dose response of the epidermal, microvascular, and dermal populations," in *Advances in Radiation Biology*, J. Lett and K. Altman, Eds., Vol. **12**, pp. 147–203, Academic Press, San Diego, California (1987).
16. J. O. Archambeau et al., "The ratio for nonhealing in swine skin: an estimate of microvessel endothelial dose tolerance," in *Presented to the 41st Annual Meeting of the Radiation Research Society* (1993).
17. J. O. Archambeau and R. M. Shymko, "Tissue population configuration as a modifier of organ dose response," *Int. J. Radiat. Oncol. Biol. Phys.* **15**(3), 727–734 (1988).
18. S. P. Steamer and E. J. B. Christian, "Mechanisms of acute injury in the gamma irradiated chicken: in vivo studies and dose protraction effect on the microvasculature," *Radiat. Res.* **47**, 741–755 (1971).
19. H. A. Van Den Brenk, "The effect of ionizing radiation on capillary sprouting and remodeling in the regenerating blastema observed in the rabbit ear chamber," *Am. J. Roentgenol. Radium. Ther. Nucl. Med.* **81**(5), 859–884 (1959).
20. D. C. White, *An Atlas of Radiation Histopathology*, Armed Forces Institute of Pathology, Washington, DC (1975).
21. M. Spalek, "Chronic radiation-induced dermatitis: challenges and solutions," *Clin. Cosmet. Investig. Dermatol.* **9**, 473–482 (2016).
22. C. M. Rowland Payne et al., "The hyfrecator: a treatment for radiation induced telangiectasia in breast cancer patients," *Br. J. Radiol.* **78**(926), 143–146 (2005).
23. A. M. Rossi, K. S. Nehal, and E. H. Lee, "Radiation-induced breast telangiectasias treated with the pulsed dye laser," *J. Clin. Aesthet. Dermatol.* **7**(12), 34–37 (2014).
24. M. Crisan et al., "Ultrasonographic staging of cutaneous malignant tumors: an ultrasonographic depth index," *Arch. Dermatol. Res.* **305**(4), 305–313 (2013).
25. J. Stefanowska, D. Zakowiecki, and K. Cal, "Magnetic resonance imaging of the skin," *J. Eur. Acad. Dermatol. Venereol.* **24**, 875–880 (2010).
26. A. L. Branzan, M. Landthaler, and R. M. Szeimies, "In vivo confocal scanning laser microscopy in dermatology," *Lasers Med. Sci.* **22**, 73–82 (2007).
27. D. Huang et al., "Optical coherence tomography," *Science* **254**(5035), 1178–1181 (1991).

28. N. D. Gladkova et al., "In vivo optical coherence tomography imaging of human skin: norm and pathology," *Skin Res. Technol.* **6**(1), 6–16 (2000).
29. E. Sattler, R. Kästle, and J. Welzel, "Optical coherence tomography in dermatology," *J. Biomed. Opt.* **18**(6), 061224 (2013).
30. T. Gambichler, V. Jaedicke, and S. Terras, "Optical coherence tomography in dermatology: technical and clinical aspects," *Arch. Dermatol. Res.* **303**(7), 457–473 (2011).
31. O. Babalola et al., "Optical coherence tomography (OCT) of collagen in normal skin and skin fibrosis," *Arch. Dermatol. Res.* **306**(1), 1–9 (2014).
32. G. Abignano et al., "Virtual skin biopsy by optical coherence tomography: the first quantitative imaging biomarker for scleroderma," *Ann. Rheum. Dis.* **72**(11), 1845–1851 (2013).
33. M. C. Pierce et al., "Birefringence measurements in human skin using polarization-sensitive optical coherence tomography," *J. Biomed. Opt.* **9**(2), 287–291 (2004).
34. A. Mariampillai et al., "Speckle variance detection of microvasculature using swept source optical coherence tomography," *Opt. Lett.* **33**(13), 1530–1532 (2008).
35. R. Clarkson et al., "Characterization of image quality and image-guidance performance of a preclinical microirradiator," *Med. Phys.* **38**(2), 845–856 (2011).
36. S. Kumar et al., "Radiation-induced skin injury in the animal model of scleroderma: implications for post-radiotherapy fibrosis," *Radiat. Oncol.* **3**, 40 (2008).
37. J. A. Horton et al., "Quercetin inhibits radiation-induced skin fibrosis," *Radiat. Res.* **180**(2), 205–215 (2013).
38. Y. Mao et al., "High-quality tissue imaging using a catheter-based swept-source optical coherence tomography systems with an integrated semiconductor optical amplifier," *IEEE Trans. Instrum. Meas.* **60**(10), 3376–3383 (2011).
39. V. Demidov et al., "Preclinical longitudinal imaging of tumor microvascular radiobiological response with functional optical coherence tomography," *Sci. Rep.* **8**(1), 1–12 (2018).
40. A. Mariampillai et al., "Optimized speckle variance OCT imaging of microvasculature," *Opt. Lett.* **35**(8), 1257–1259 (2010)
41. H. Assadi et al., "Microvascular contrast enhancement in optical coherence tomography using microbubbles," *J. Biomed. Opt.* **21**(7), 076014 (2016)
42. .J. M. Fitzpatrick and M. Sonka, Eds., *Handbook of Medical Imaging, Volume 2. Medical Image Processing and Analysis*, SPIE Press, Bellingham, Washington (2000).
43. N. Otsu, "A threshold selection method from gray-level histograms," *IEEE Trans. Syst. Man Cybernet.* **9**(1), 62–66 (1979).
44. A. E. Carpenter et al., "CellProfiler: image analysis software for identifying and quantifying cell phenotypes," *Genome Biol.* **7**(10), R100 (2006).
45. T. Gambichler et al., "In vivo data of epidermal thickness evaluated by optical coherence tomography: effects of age, gender, skin type, and anatomic site," *Dermatol. Sci.* **44**(3), 145–152 (2006).
46. Y. Liew et al., "In vivo assessment of human burn scars through automated quantification of vascularity using optical coherence tomography," *J. Biomed. Opt.* **18**(6), 061213 (2013).
47. J. O. Archambeau, R. Pezner, and T. Wasserman, "Pathophysiology of irradiated skin and breast," *Int. J. Radiat. Oncol. Biol. Phys.* **31**(5), 1171–1185 (1995).
48. H. Goldschmidt, J. C. Breneman, and D. L. Breneman, "Ionizing radiation therapy in dermatology," *J. Am. Acad. Dermatol.* **30**(2), 157–182 (1994).
49. R. G. Panizzon and M. H. Seegenschmiedt, *Radiation Treatment and Radiation Reactions in Dermatology*, 2nd ed., Springer-Verlag, Berlin (2015).
50. R. A. Byers et al., "Vascular patterning of subcutaneous mouse fibrosarcomas expressing individual VEGF isoforms can be differentiated using angiographic optical coherence tomography," *Biomed. Opt. Express.* **8**(10), 4551–4567 (2017).
51. S. Schultze-Mosgau et al., "Vascularization of the area between free grafts and irradiated graft beds in the neck in rats," *Br. J. Oral Maxillofac. Surg.* **40**(1), 37–44 (2002).
52. B. Davoudi et al., "Quantitative assessment of oral microstructural and microvascular changes in late oral radiation toxicity, using noninvasive in-vivo optical coherence tomography," *Photon. Lasers. Med.* **5**, 21–32 (2015).
53. A. V. Maslennikova et al., "In-vivo longitudinal imaging of microvascular changes in irradiated oral mucosa of radiotherapy cancer patients using optical coherence tomography," *Sci. Rep.* **7**(16505), 1–10 (2017).
54. A. Moiseev et al., "Optical coherence tomography-based angiography device with real-time angiography B-scans visualization and hand-held probe for every-day clinical use," *J. Biophotonics* e201700292 (2018).
55. L. Pires et al., "Optical clearing of melanoma in vivo: characterization by diffuse reflectance spectroscopy and optical coherence tomography," *J. Biomed. Opt.* **21**(8), 081210 (2016).

Biographies for the authors are not available.